KSME

Springer

Journal of Mechanical Science and Technology 36 (5) 2022

Original Article
DOI 10.1007/s12206-022-0423-0

Keywords:
· Centrifugal compressor
· Computational fluid dynamics (CFD)
· Impeller-diffuser interaction (IDI)
· Unsteady flow
· URANS

Correspondence to:
Seung Jin Song
sjsong@snu.ac.kr

Citation:
Kong, D., Song, S. J. (2022). Influence of flow coefficient on unsteady impeller loading induced by impeller-diffuser interaction. Journal of Mechanical Science and Technology 36 (5) (2022) 2403~2413.
http://doi.org/10.1007/s12206-022-0423-0

Received September 27th, 2021
Revised January 13th, 2022
Accepted January 24th, 2022

† Recommended by Editor
Yang Na

Influence of flow coefficient on unsteady impeller loading induced by impeller-diffuser interaction

Dongjae Kong[1] and Seung Jin Song[2]

[1]Department of Mechanical Engineering, Stanford University, Stanford 94305, United States, [2]Institute of Advanced Machines and Design, Seoul National University, Seoul 08826, Korea

Abstract Unsteady Reynolds-averaged Navier-Stokes (URANS) simulation has been conducted to investigate how the flow coefficient affects unsteady impeller loading. Simulations have been carried out at three flow coefficients - near stall, design, and near choke conditions - for a centrifugal compressor with a radial gap of 1.04. For computational efficiency, the unsteady simulation has been conducted for two impeller and diffuser passages via the Fourier transformation method. Unsteady loading is the largest at the near stall condition; second largest at the near choke condition; and smallest at the design condition. Relative to the design condition, the near stall condition shows lower minimum loading, and the near choke condition shows higher maximum loading. Thus, both off-design conditions result in higher unsteady loading than at the design condition. Such increases at off-design conditions stem from the variations in the pitch-wise static pressure at the diffuser vane inlet caused by the diffuser vane incidence.

1. Introduction

Centrifugal compressors are widely used in various industries, including aircraft propulsion, automotive transportation, and process applications. Compared to axial machines, centrifugal compressors are more compact and achieve higher pressure rise per stage. A centrifugal compressor stage consists of an impeller and diffuser, and the diffuser may be vaned or vaneless. While diffuser vanes enhance pressure rise and efficiency, the relative motion between the rotating impeller and stationary diffuser vanes leads to impeller-diffuser interaction (IDI). So far, IDI has been studied mostly from the aerodynamic performance perspective [1-3]. However, the potential effect of the diffuser vane imposes a non-uniform pressure field in the space between the impeller and diffuser, resulting in an unsteady loading for the rotating impeller blades. Therefore, the impeller is subject to the unsteady as well as static loading, and thus can become susceptible to vibration.

Aerodynamic studies on unsteady impeller loading induced by IDI in high-speed centrifugal compressors are as follows. Gaetani et al. [4, 5] measured unsteady static pressure, Mach number, and flow angle in the space between the impeller and diffuser using fast response aerodynamic pressure probes. Smythe [6] numerically investigated unsteady impeller loading in two different compressors at two flow coefficients (near design and lower than the design flow coefficients). One compressor had a larger impeller tip radius and a smaller radial gap than the other. The impeller with a smaller radial gap (between the impeller and the diffuser) showed increased unsteady loading on the impeller, and such unsteady loading was concentrated at the trailing edge of the blade. Smythe also reported that unsteady impeller loading decreased at higher flow coefficients. For the same geometries and operating conditions, Villanueva [7] reported that the unsteady impeller loading is set by the “difference in static pressure from the pressure surface to the suction surface at the leading edge of the diffuser vane”, and the difference increases as the diffuser vane incidence decreases or flow coefficient increases. In a

centrifugal compressor different from those in Refs. [6, 7], Gould et al. [8] conducted a quasi-two-dimensional numerical simulation and reported that the downstream disturbance induced by the diffuser vane was attenuated more rapidly when the relative Mach number inside the impeller passage increased.

Structural studies have been carried out as well. Zemp and Abhari [9] measured impeller blade stress levels induced by IDI using dynamic strain gauges. The stress measurements were conducted at the design and off-design (near stall and near choke) conditions for two radial gaps of 1.08 and 1.13. The maximum stress level decreased with increasing flow coefficient for the large radial gap (1.13). However, for the smaller radial gap (1.08), the maximum stress levels were larger at both off-design conditions relative to the design condition.

Based on the investigation at two flow coefficients (near design and lower than the design flow coefficients), Smythe [6] found that the unsteady impeller loading decreases as the flow coefficient increases. According to Villanueva [7], unsteady impeller loading can be expected to continuously decrease as the flow coefficient increases to near choke condition. However, Zemp and Abhari [9] found that the maximum impeller stress can have a local minimum at the design condition, implying that the unsteady impeller loading can also have a local minimum at the design condition. Yet, this is inconsistent with Villanueva [7], which expected a continuous decrease of unsteady impeller loading with increasing flow coefficient. Given such different results, there is still a need to physically understand the effects of the flow coefficient (ranging from near stall to design to near choke conditions) on the unsteady impeller loading induced by IDI in a high-speed compressor. Therefore, this paper presents results from a numerical investigation aiming to answer the following research questions.

1) How does the flow coefficient affect unsteady impeller loading?

2) What fluid dynamic phenomenon is mainly responsible for the unsteady impeller loading?

2. Test compressor

2.1 Geometry

The current numerical study has been conducted on the open test case “Radiver”. The measurements on the test case were carried out at the Institute of Jet Propulsion and Turbomachinery at RWTH Aachen, Germany. Part of the investigations was funded by the Deutsche Forschungsgemeinschaft (DFG) [1, 2]. Fig. 1 is the frontal view of the centrifugal compressor. It is composed of an unshrouded impeller with 15 backswept main blades and 23 wedge-type diffuser vanes. For the current study, diffuser vane angle, α_{4SS}, and radial gap, r_4/r_2, are 16.5° and 1.04, respectively. Geometrical specifications are summarized in Table 1. The design point and other test conditions based on the experiments [1, 2] are listed in Table 2. Flow coefficients of 0.2073, 0.2232, and 0.2362 corresponding to near stall, design, and near choke conditions, respectively, have been analyzed.

Table 1. Geometrical specifications [1].

Impeller	
Tip radius, r_2 (mm)	135
Number of blades, N_I	15
Blade back-sweep angle at the exit, β_b (deg)	38
Diffuser	
Height, b (mm)	11.1
Number of vanes, N_D	23
Diffuser vane angle, α_{4SS} (deg)	16.5
Radial gap, r_4/r_2	1.04
Diffuser vane wedge angle, α_{DV} (deg)	6.615
Length of vane pressure side, L_{DVPS} (mm)	178
Length of vane suction side, L_{DVSS} (mm)	190

Table 2. Test conditions [1].

Shaft speed, N (RPM)	28160
Impeller tip speed, U_{tip} (m/s)	398.4
Near stall flow coefficient	0.2073
Design flow coefficient	0.2232
Near choke flow coefficient	0.2362

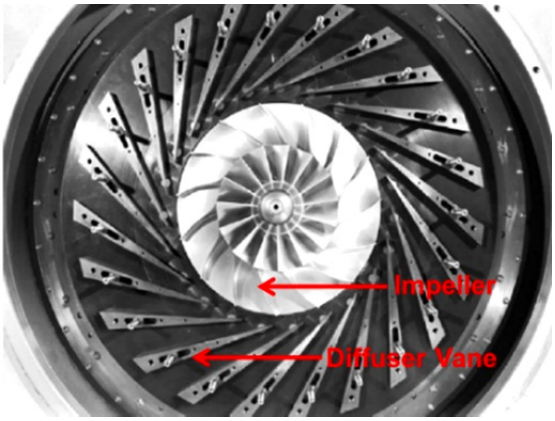

Fig. 1. Frontal view of the centrifugal compressor stage [1].

2.2 Measurements

Measurement methods from “Radiver” are briefly cited here. Although steady and unsteady measurements were conducted extensively at various locations, only the measurement locations relevant to the current study are described. Figs. 2(a) and (b) represent the frontal and the meridional views of measurement planes, respectively. Steady measurements at the 8M location were conducted with a 3-hole cylinder probe, temperature probe, and pressure taps. Unsteady measurements at the 4M location were conducted using the time-resolved laser-2-focus technique. Aforementioned measurements were conducted at 80 % of the shaft speed, and, thus, numerical simula-

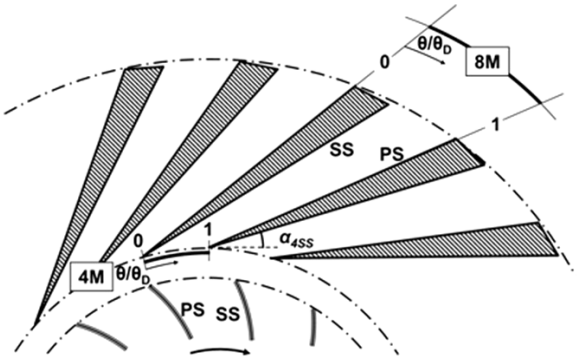

(a) Frontal view

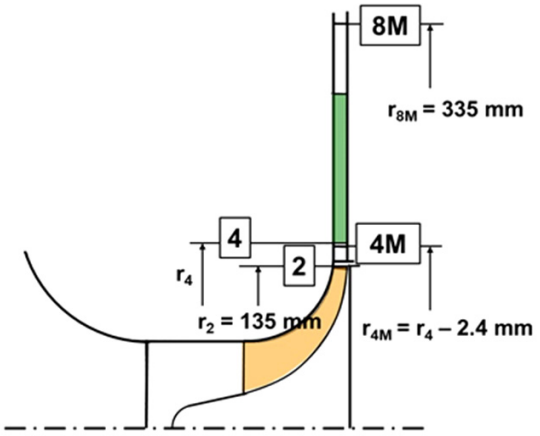

(b) Meridional view

Fig. 2. Measurement planes [1, 2].

tion of the current study has been conducted at the same shaft speed. More details of the test rig and measurement techniques can be found in Refs. [1, 2].

3. Numerical method

3.1 Grid

Computational domain and grid have been generated using ANSYS Turbogrid 17.0. Inlet of the computational domain is located at a distance of twice the impeller leading edge tip radius upstream from the impeller leading edge. Diffuser vane exit and outlet radii are located at 1.97 and 2.67 times the impeller trailing edge tip radius, respectively. The collector has not been modeled. Locations of the inlet and the outlet have been selected to minimize the effects of boundaries on the computation. A structured and hexahedral grid has been adopted. The tip clearance of the current impeller is uniformly 0.7 mm when cold. However, as the compressor accelerates, centrifugal force and hot air affect tip clearance distribution, and Ziegler [10] predicted the hot condition tip clearance distribution via FEM analysis. The current study has adopted the linear tip clearance distribution suggested in Ref. [10], and, thus, tip clearances at the leading and the trailing edges have been set at 0.69 mm and 0.48 mm, respectively.

3.2 Numerical methods

Both steady and unsteady three-dimensional Reynolds-averaged Navier-Stokes (RANS) simulations have been carried out using ANSYS CFX 17.0. Steady simulations have been conducted to obtain the initial condition for the unsteady simulation. Uniform total pressure and total temperature have been imposed at the inlet boundary. In addition, the inlet flow direction and turbulence intensity of 5 % have been imposed. The mass flow rate has been set at the outlet boundary, and air as ideal gas has been used as the working fluid. Total energy modeling has been adopted for the temperature calculation, and viscous work has been included. Wall has been modeled as an adiabatic smooth surface with no slip. Shear stress transport (SST) model has been utilized, and y+ of the near-wall grid has been maintained around unity. Flow has been assumed to be fully turbulent.

Steady simulation has been conducted for a single passage of the impeller and the diffuser. Rotationally periodic boundary conditions have been imposed on the pitch-wise periodic interfaces for the impeller and the diffuser. The impeller-diffuser interface has been modeled via the mixing plane method. The interface is equidistant from the impeller trailing edge and the diffuser vane leading edge. For the current simulation where the flow is complex and separated, root mean square (RMS) of the residuals below 5E-5 has been selected as a converged solution.

Using the steady simulation results as the initial condition, unsteady simulations have been conducted. As the pitch ratio between the impeller and the diffuser is not unity (15/23), the transient blade row model and Fourier transformation method have been applied. Thus, two passages of the impeller and the diffuser have been modeled. More detailed technical discussions on the transient blow row model and Fourier transformation method can be found in Refs. [11, 12]. The time step for the unsteady simulation has been set to be 1/30 of the diffuser vane pitch. In the unsteady simulations, in addition to the residuals' RMS, periodicity coefficients (Eq. (1)) under 0.5 % have also been used as convergence criteria. Periodicity coefficients have been evaluated at six points near the impeller trailing edge (pressure side and suction side at 10 %, 50 %, and 90 % span-wise locations, respectively).

$$Periodicity\ coefficient\ [\%] = \frac{P(r,\theta,z,t+T)-P(r,\theta,z,t)}{P(r,\theta,z,t)}\times 100. \quad (1)$$

3.3 Numerical method validation

Fig. 3 shows plots of the total pressure ratio versus the grid number. For three flow coefficients, the total pressure ratio from the inlet to the 8M location (Fig. 2) has been investigated for various grid numbers. Grid number is the sum of the grids in the single passage of the impeller and the diffuser. At all flow coefficients, the differences in the predicted total pressure ra-

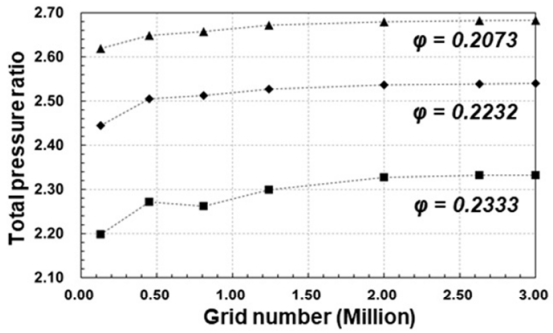

Fig. 3. Grid dependence results.

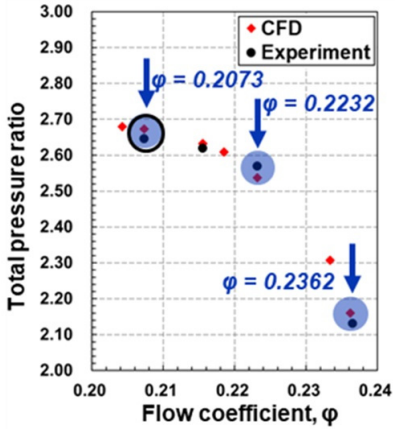

(a) Total pressure ratio

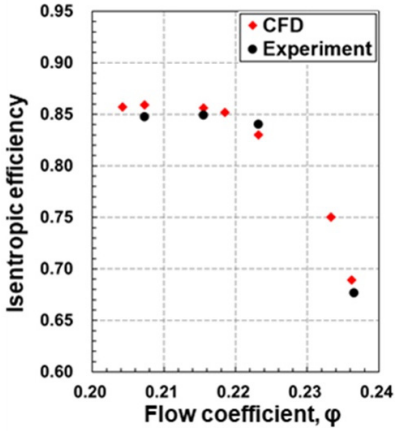

(b) Isentropic efficiency

Fig. 4. Comparison of compressor map: (a) total pressure ratio; (b) isentropic efficiency.

tios between grid numbers of 2.0 million and 3.0 million are negligible. Therefore, the current study has been conducted at a grid number of 2.0 million. The impeller passage is composed of approximately 1.3 million grids, and the diffuser passage is composed of around 0.7 million grids.

To validate current numerical methods, steady simulation results have been compared against experimental data. Figs. 4(a) and (b) show comparisons of the predicted and measured total pressure ratios and isentropic efficiencies, respectively.

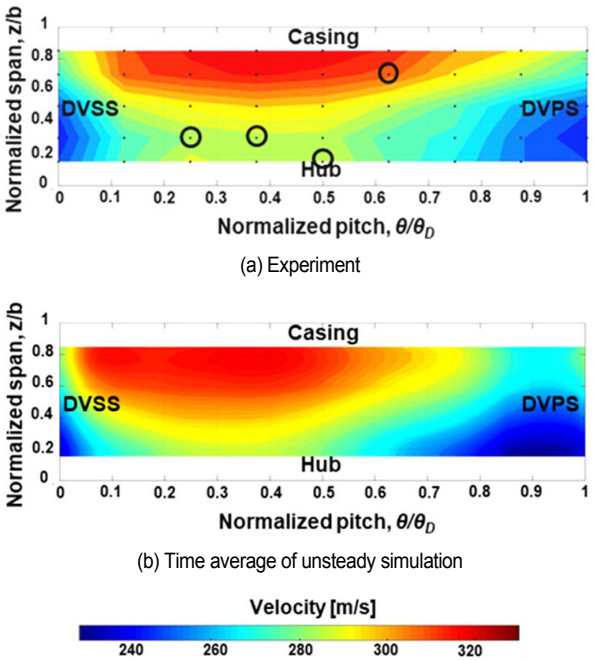

(a) Experiment

(b) Time average of unsteady simulation

Fig. 5. Diffuser vane inlet time-averaged velocity contours at 4M: (a) measured; (b) predicted.

Total pressure ratio and isentropic efficiency are defined in Eqs. (2) and (3), respectively. Predictions from the steady simulation match with the experimental data to within 1.5 %. Flow coefficients selected for unsteady analysis are indicated by the blue circles in Fig. 4(a).

$$\pi_{tc} = Mass\ averaged\ P_t(Plane\,8M) / P_t(\mathrm{Im}\ peller\ inlet)\ , \quad (2)$$

$$\eta_c = (\pi_{tc}^{\gamma-1/\gamma} - 1) / (\tau_{tc} - 1)$$

$$\tau_{tc} = Mass\ averaged\ T_t(Plane\,8M) / T_t(\mathrm{Im}\ peller\ inlet)\ . \quad (3)$$

The unsteady analysis has been validated as follows. Figs. 5(a) and (b) show time-averaged absolute velocity contours from the experiment and unsteady simulation, respectively, at the diffuser vane inlet for φ = 0.2073 (Fig. 4(a)). The vertical axis is the span-wise location, and the horizontal axis is the pitch-wise location. Hub and casing correspond to z/b = 0 and 1, respectively, and diffuser vane suction side (DVSS) and pressure side (DVPS) correspond to θ/θ_D = 0 and 1, respectively. Measurement locations are from the 4M plane in Fig. 2. Fig. 5(a) shows the measured velocity as well as the measurement locations (black dots), and Fig. 5(b) presents the predicted velocity. The high-velocity region (near the diffuser vane suction side and the casing) and low-velocity region (near the diffuser vane pressure side and the hub) are well simulated. Huang et al. [13] also predicted such high and low-velocity regions using a commercial code.

Figs. 6(a)-(d) show the measured and predicted velocity variations versus normalized time at four circled measurement points in Fig. 5(a). Each measurement location has been indicated below each plot by normalized pitch-wise and normal-

ized span-wise coordinates. Velocity variation is defined in Eq. (4) as the difference between the local instantaneous velocity and the local time-averaged velocity normalized by the local time-averaged velocity. At all four measurement points, temporal velocity variations are well predicted via unsteady simulation.

$$Velocity\ \mathrm{var}iation = \left[C(\theta/\theta_D, z/b, t) - \bar{C}(\theta/\theta_D, z/b)\right] / \bar{C}(\theta/\theta_D, z/b) . \quad (4)$$

Lack of unsteady pressure data from "Radiver" prevents unsteady pressure comparison. Nevertheless, from the steady and unsteady velocity validations, the numerical methods can be judged to be reliable.

4. Results and discussions

4.1 Unsteady loadings

Figs. 7(a)-(c) show the chord-wise distributions of unsteady loading per unit span at 10 %, 50 %, and 90 % span-wise locations, respectively. Loading is defined in Eq. (5) as the difference in static pressure per unit span between the impeller blade pressure and suction sides; and unsteady loading per unit span is defined in Eq. (6) as the difference between the maximum and the minimum loadings for a single diffuser passage period normalized by the dynamic pressure based on the impeller tip speed. At all span-wise locations, unsteady loading is the largest near the trailing edge and negligible for chord-wise locations less than 0.5. Furthermore, at all span-wise locations, the maximum unsteady loading is detected at around 0.98 chord-wise location. The maximum unsteady loading is the largest at near stall, second largest at near choke, and smallest at the design condition. Table 3 summarizes the maximum unsteady loading at three flow coefficients and three span-wise locations. Maximum unsteady loading decreases from the hub to the shroud regardless of the flow coefficient. A similar span-wise variation has also been reported by Smythe [6] and Villanueva [7]. Since the unsteady loadings at three span-wise locations are similar, further investigation has been focused on the 10 % span-wise location (near the hub).

Table 3. Maximum unsteady loading at three flow coefficients and three span-wise locations.

	Near stall	Design	Near choke
10 % span (near hub)	0.4394	0.3187	0.3914
50 % span (mid span)	0.3967	0.2842	0.3707
90 % span (near shroud)	0.3396	0.2593	0.3236

$$Loading, \quad \Delta P = P_{PS} - P_{SS} , \quad (5)$$

$$Unsteady\ loading = (\Delta P_{\max} - \Delta P_{\min}) / 0.5\rho U_{tip}^2 . \quad (6)$$

To determine the frequency contents of the unsteady loading, fast Fourier transformation (FFT) analysis has been conducted.

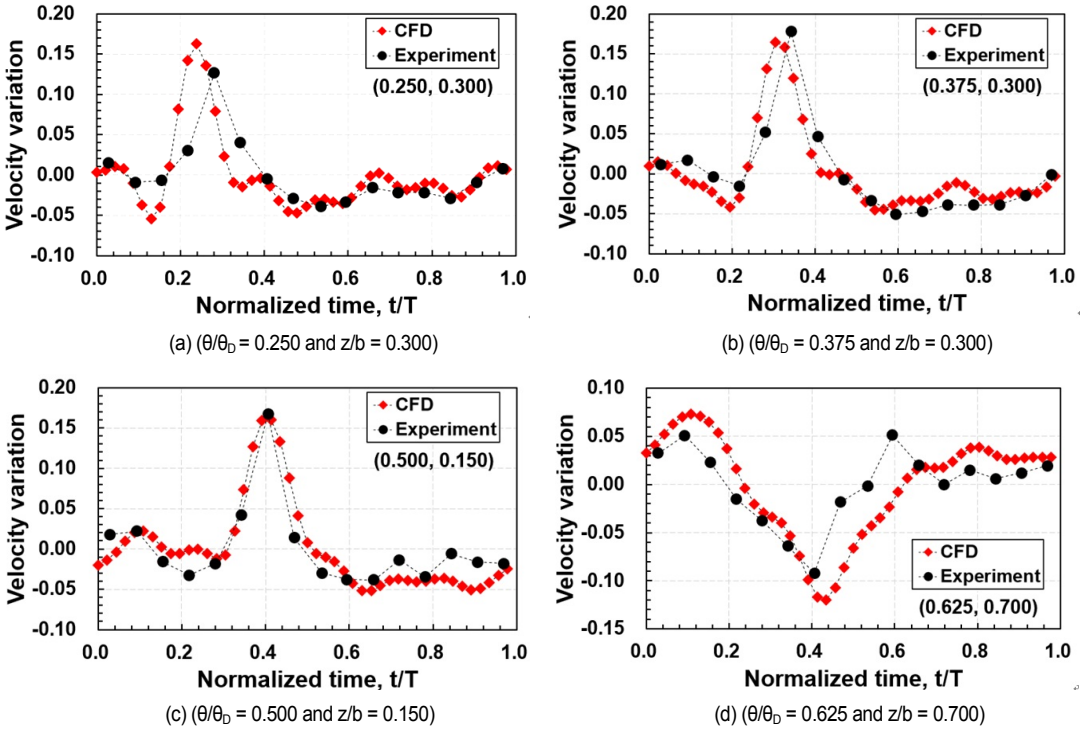

(a) (θ/θ_D = 0.250 and z/b = 0.300)

(b) (θ/θ_D = 0.375 and z/b = 0.300)

(c) (θ/θ_D = 0.500 and z/b = 0.150)

(d) (θ/θ_D = 0.625 and z/b = 0.700)

Fig. 6. Diffuser vane inlet velocity variations with respect to time at four measurement points.

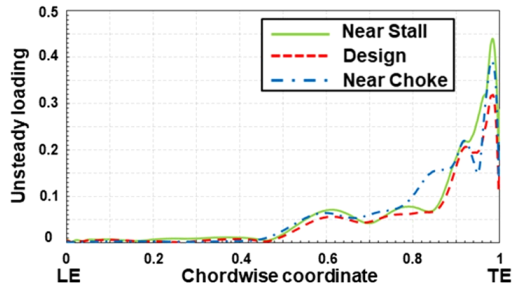

(a) 10 % span (near hub)

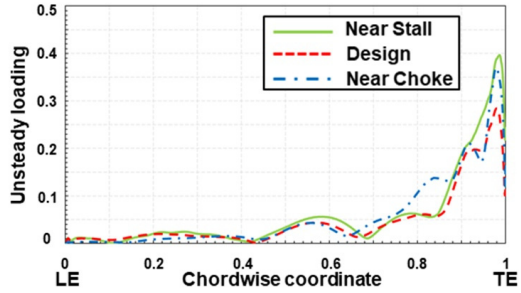

(b) 50 % span (mid span)

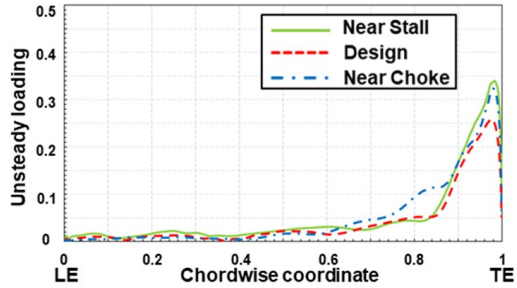

(c) 90 % span (near shroud)

Fig. 7. Chord-wise distributions of unsteady loading per unit span at (a) 10 % span; (b) 50 % span; (c) 90 % span.

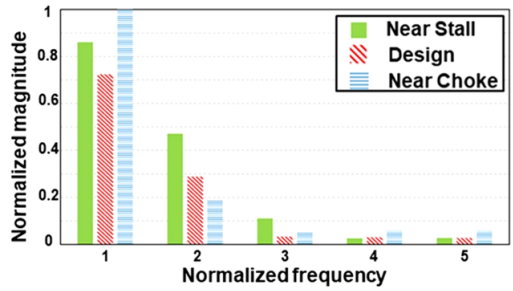

Fig. 8. Frequency contents of the unsteady loading at 0.98 chord-wise location.

Fig. 8 shows the FFT results of the unsteady loading at 0.98 chord-wise location (where the maximum unsteady loading has been detected) for the three flow coefficients. The frequency has been normalized by the diffuser vane passing frequency, and the magnitude has been normalized by the maximum magnitude. For all three flow coefficients, 1) the first two harmonics are dominant; and 2) the first harmonic magnitudes are about twice those of the second harmonic. Thus, the dominant frequency of the unsteady loading is the diffuser vane passing frequency.

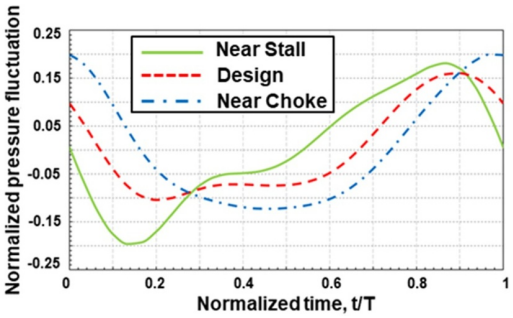

(a) Pressure side pressure fluctuations

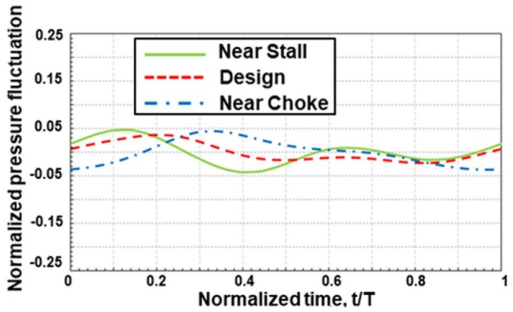

(b) Suction side pressure fluctuations

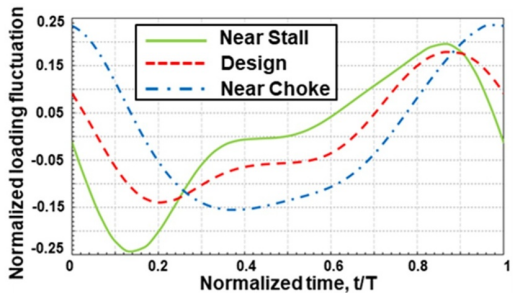

(c) Loading fluctuations

Fig. 9. Temporal variation of (a) pressure side pressure fluctuations; (b) suction side pressure fluctuations; (c) loading fluctuations at 0.98 chord-wise location.

The loading is a function of the pressures on the pressure and the suction sides, and unsteady loading is determined by the maximum and the minimum loadings. Therefore, temporal variations of pressure and loading have been examined. Figs. 9(a)-(c) show the temporal variation of fluctuations in the pressure side pressure (Fig. 9(a)), suction side pressure (Fig. 9(b)), and loading (Fig. 9(c)) at the 0.98 chord-wise location for the three flow coefficients. Normalized fluctuations on the pressure and the suction side pressures and loading are defined in Eqs. (7)-(9), respectively.

$$C_{P,PS}(s,t)' = \left(P_{PS}(s,t) - \overline{P_{PS}(s)}\right) / 0.5\rho U_{tip}^2 \quad (7)$$

$$C_{P,SS}(s,t)' = \left(P_{SS}(s,t) - \overline{P_{SS}(s)}\right) / 0.5\rho U_{tip}^2 \quad (8)$$

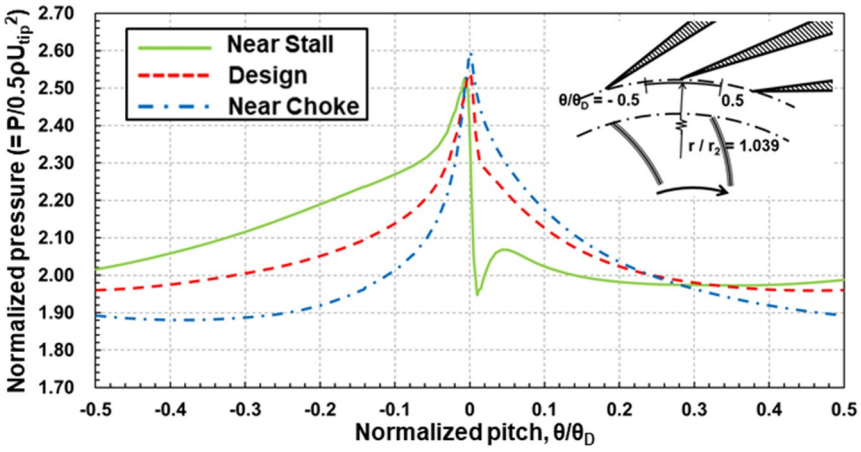

Fig. 10. Pitch-wise time-averaged static pressure distributions at r/r_2 = 1.039.

$$C_{\Delta P}(s,t)' = \left(\Delta P(s,t) - \overline{\Delta P(s)}\right) / 0.5\rho U_{tip}^2 . \quad (9)$$

The unsteady loading varies with flow coefficient mainly due to the fluctuations on the pressure side. For the design condition, the minimum loading occurs at t/T = 0.2, which coincides with the time when the minimum pressure occurs on the pressure side. Likewise, the maximum loading occurs at t/T = 0.86, which is close to the moment when the maximum pressure appears on the pressure side, t/T = 0.89. For the near stall condition, the maximum pressure on the pressure side remains similar to that at the design condition, but the minimum pressure on the pressure side is lower than that at the design condition. Consequently, the near stall condition has a higher unsteady loading (Eq. (6)) than the design condition. On the other hand, relative to the design condition, the near choke condition has a higher maximum pressure and a similar minimum pressure on the pressure side. Thus, the near choke condition also has a higher unsteady loading than the design condition.

4.2 Time averaged pressure distributions

Pressure and loading fluctuations on the impeller blade in Fig. 9 are significantly affected by the pressure near the diffuser vane inlet. Therefore, the pitch-wise pressure distribution at the diffuser vane inlet has been examined, and Fig. 10 shows the pitch-wise time-averaged non-dimensional static pressure distributions at r/r_2 = 1.039 for three flow coefficients. Pressure increases from θ/θ_D = -0.5 (between diffuser vane leading edges) to θ/θ_D = 0 (diffuser vane leading edge). At the near stall condition, pressure near the diffuser vane leading edge is similar to that of the design condition. Since the maximum loading is set by the high pressure near the diffuser vane leading edge, the maximum loadings of two conditions are similar (Fig. 9(c)). However, compared to the design condition, pressure drops more rapidly after the impeller blade passes by the diffuser vane leading edge. Minimum loading occurs when the high pressure imposed on the impeller blade pressure side drops rapidly; thus, the near stall condition has a lower minimum loading (Fig. 9(c)).

Conversely, relative to the design condition, pressure near the diffuser vane leading edge is higher at the near choke condition. Thus, higher pressure is imposed on the impeller blade pressure side, resulting in a higher maximum loading (Fig. 9(c)). After the impeller blade passes by the diffuser vane leading edge, pressure decreases in the pitch-wise direction are similar at both the design and near choke conditions, leading to similar minimum loadings (Fig. 9(c)).

Variations in the pitch-wise pressure distributions in Fig. 10 are set by the diffuser vane inlet pressure fields. Figs. 11(a)-(c) show the non-dimensional time-averaged diffuser vane inlet pressure fields at near stall (Fig. 11(a)), design (Fig. 11(b)), and near choke (Fig. 11(c)) conditions. Pressure contour near the diffuser vane leading edge is symmetric about the diffuser vane centerline at the near stall condition. However, as the flow coefficient increases, the stagnation point moves increasingly toward the suction side of the diffuser vane leading edge, and the pressure field becomes asymmetric. Gaetani et al. [5] and Liu et al. [14] reported a similar trend. Such changes stem from decreasing incidence as the flow coefficient increases.

Table 4 summarizes time and mass averaged diffuser vane incidence for the three flow coefficients. Diffuser vane incidence is defined as the difference between the flow angle and the diffuser vane centerline angle at the vane inlet. Incidence has been taken as positive when its direction is identical to the impeller rotating direction (Fig. 12). Thus, as the flow coefficient increases, incidence decreases, and the impeller exit absolute velocity becomes more radial (Fig. 12), altering the diffuser vanes' potential field and pitch-wise pressure distribution.

Villanueva [7] suggested that the "difference in static pressure from the pressure surface to the suction surface at the leading edge of the diffuser vane" sets the unsteady impeller loading. According to Villanueva, the difference increases as the diffuser vane incidence decreases or flow coefficient increases (Fig. 12). If so, the unsteady impeller loading is expected to continuously decrease as the flow coefficient in-

Table 4. Time and mass averaged diffuser vane incidence at three flow coefficients.

Flow coefficient	Incidence (deg)
Near stall	- 1.42
Design	- 3.92
Near choke	- 6.35

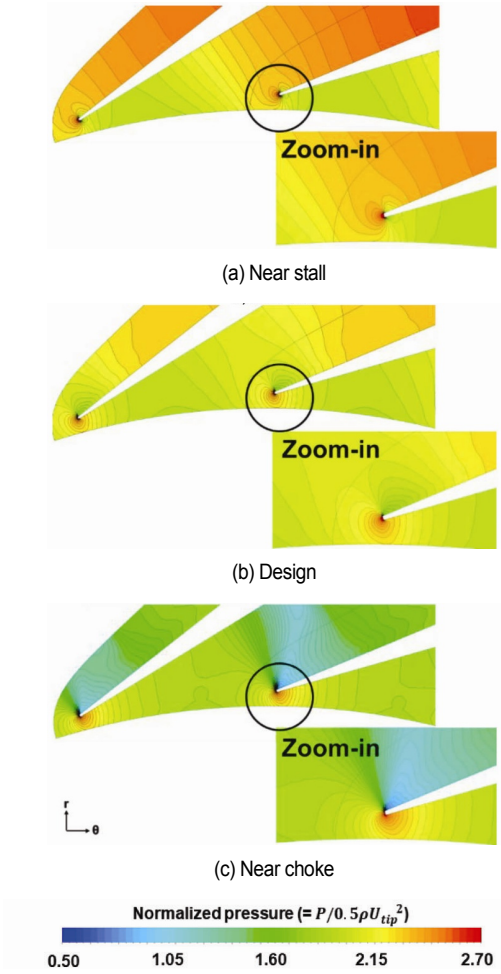

Fig. 11. Time-averaged diffuser vane inlet pressure fields at (a) near stall; (b) design; (c) near choke conditions.

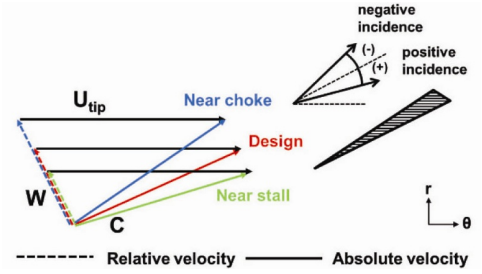

Fig. 12. Velocity triangles of impeller exit flow at three flow coefficients.

creases to near choke condition. However, the current study finds that i) the unsteady impeller loading can have a local minimum at the design condition; and ii) the pitch-wise static

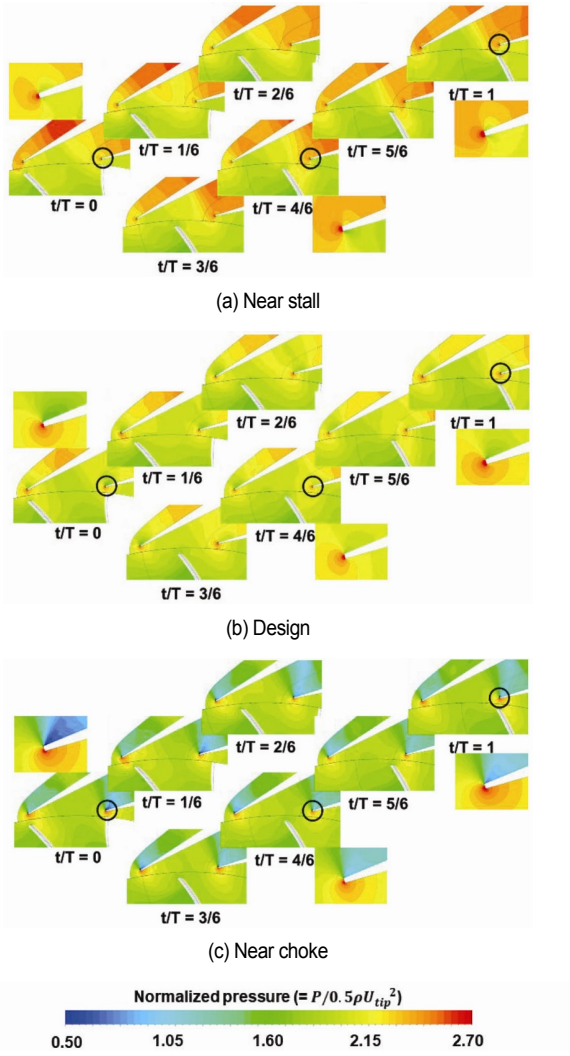

Fig. 13. Unsteady pressure fields for one impeller passage at (a) near stall; (b) design; (c) near choke conditions.

pressure distribution near the diffuser vane leading edge influences the unsteady impeller loading.

4.3 Unsteady flow fields

Figs. 13(a)-(c) present the pressure fields at six instances for the three flow coefficients, and pressure has been normalized by the dynamic pressure based on the impeller tip speed. Pressure fields in the vaneless space change with time due to the IDI, and such variation depends on the flow coefficient. Nevertheless, at all times, pressure contours near the diffuser vane leading edge remain symmetric about the diffuser vane centerline at the near stall condition (Fig. 13(a)). At the near choke condition, the stagnation point moves toward the suction side of the diffuser vane leading edge, and the pressure fields remain asymmetric at all times (Fig. 13(c)).

Regardless of the flow coefficient, the pressure on the impeller blade pressure side increases as the impeller blade approaches the diffuser vane. Maximum unsteady loadings in Fig.

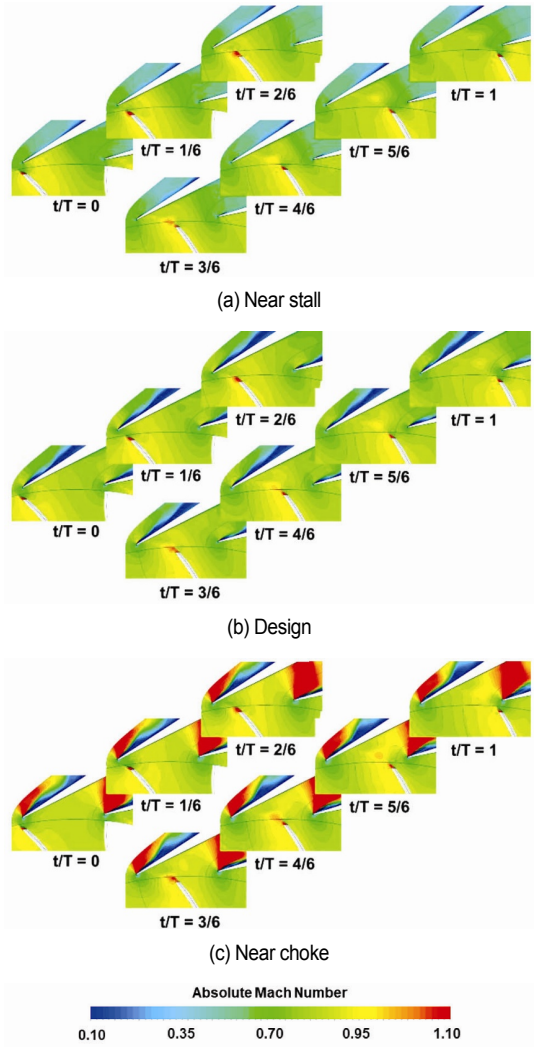

Fig. 14. Unsteady absolute Mach number fields for one impeller passage at (a) near stall; (b) design; (c) near choke conditions.

9 can be found in Fig. 13 at t/T = 5/6 for the near stall and the design conditions and t/T = 1 for the near choke condition. After passing the diffuser vane, high pressure on the impeller blade pressure side is diminished, resulting in a reduced blade loading. At the same time, the impeller blade suction side moves away from the high-pressure region near the diffuser vane leading edge, and, thus, pressure fluctuation on the impeller blade suction side is negligible (Fig. 9(b)). Minimum loadings in Fig. 9 can be found in Fig. 13 at t/T = 1/6 for the near stall and the design conditions and t/T = 2/6 for the near choke condition.

Figs. 14(a)-(c) present the corresponding absolute Mach number fields at six instances for the three flow coefficients, and Mach number has been calculated based on the local speed of sound. The jet-wake model of Dean and Senoo [15] describes a low-velocity region in the relative frame (a high-velocity region in the absolute frame) near the impeller blade suction side. Schleer and Abhari [16] reported a blade trailing edge wake region (marked by low radial velocity and high tangential velocity), and described it as a high-velocity region in the absolute frame. Current unsteady simulation shows similar flow features.

After the impeller blade passes the diffuser vane, the velocity near the impeller blade suction side is accelerated (from t/T = 1/6 to t/T = 5/6). Compared to the near stall condition, the accelerated flow region near the impeller blade suction side becomes wider at the near choke condition. However, as the impeller blade approaches the diffuser vane, the flow near the impeller blade suction side is decelerated (from t/T = 5/6 to t/T = 1).

In addition, the blade trailing edge wake changes with time due to IDI. As the impeller blade approaches the diffuser vane, the extent of the wake is suppressed by the diffuser vane (from t/T = 5/6 to t/T = 1), and after passing the diffuser vane, wake is dissipated (from t/T = 0 to 5/6). However, as the flow coefficient increases, the absolute velocity of the wake increases. At the near choke condition, the Mach number of the wake reaches around 0.97 near the diffuser vane throat. Such phenomena stem from the flow acceleration, which is described in the following section.

At the near stall condition, flow is attached to the diffuser vane surface (Fig. 14(a)). However, at the design and the near choke conditions, flow is largely separated from the pressure side of the diffuser vane (Figs. 14(b) and (c)). As the flow coefficient increases, incidence decreases; the impeller exit absolute velocity becomes more radial (Fig. 12), inducing flow separation on the diffuser vane pressure side. As more radial flow induces a larger separation, the extent of the separation is expected to be larger at the near choke condition than at the design condition. Yet, at the near choke condition, flow is accelerated, and choke occurs near the diffuser vane throat. In contrast, at the near stall and the design conditions, flow is decelerated, and pressure increases from the impeller exit to the diffuser vane throat. Such flow acceleration at the near choke condition increases the momentum of the flow near the diffuser vane pressure side and reduces the extent of separation. Consequently, both the design and the near choke conditions have a similar extent of separation on the diffuser vane pressure side.

5. Conclusions

The objective of the current study is to numerically investigate the influence of flow coefficient on the unsteady impeller loading in a high-speed compressor. For the test compressor, new findings from this study are as follows:

1) The unsteady loading is the largest at the near stall condition; second largest at the near choke condition; and smallest at the design condition.

2) Pressure fluctuation on the pressure side is mostly responsible for the dependence of unsteady impeller loading on the flow coefficient.

3) At the near stall condition, high pressure imposed on the impeller blade pressure side decays more rapidly than at the

design condition. Therefore, near stall condition has a lower minimum loading and a higher unsteady loading than at the design condition.

4) At the near choke condition, higher pressure is imposed on the impeller blade pressure side than at the design condition. Consequently, the near choke condition has a higher maximum loading and a higher unsteady loading than at the design condition.

5) Such variations stem from pitch-wise static pressure distribution and the potential field at the diffuser vane inlet which are determined by the incidence at the diffuser vane.

Acknowledgments

Financial support from Hanwha Power Systems Co., Ltd. and the Seoul National University Institute of Advanced Machines and Design (SNU-IAMD) are gratefully acknowledged by the authors. The authors are also grateful to Dr. Hönen and the Institute of Jet Propulsion and Turbomachinery at RWTH Aachen, Germany, for making available the "Radiver" test data.

Parts of this paper have been presented at ASME Turbo Expo 2018 (GT2018-75584), entitled "Influence of flow coefficient on the unsteady impeller loading induced by the impeller-diffuser interaction".

Nomenclature

b : Diffuser vane height, mm
C : Absolute velocity, m/s
C_p : Static pressure coefficient
DV : Diffuser vane
L_{DVPS} : Length of vane pressure side, mm
L_{DVSS} : Length of vane suction side, mm
N : Shaft speed, RPM
N_D : Diffuser vane number
N_I : Impeller blade number
P : Pressure, Pa
PS : Pressure side
P_T : Total pressure, Pa
Q : Volume flow rate, m^3/sec
r : Radial coordinate (= radius)
s : Stream-wise coordinate (= chord-wise coordinate)
SS : Suction side
T : Diffuser vane passing period, sec
t : Time, sec
T_t : Total temperature, K
U_{tip} : Impeller tip speed, m/s
W : Relative velocity, m/s
Z : Axial coordinate
α_{4SS} : Diffuser vane angle, deg
α_{DV} : Diffuser vane wedge angle, deg
β_b : Impeller back-sweep angle at the exit, deg
γ : Specific heat ratio
ΔP : Loading (= P_{PS}-P_{SS}), Pa
η_c : Isentropic efficiency
θ : Circumferential coordinate
Θ_d : Diffuser vane pitch, deg
π_{tc} : Total pressure ratio
ρ : Density, kg/m^3
τ_{tc} : Total temperature ratio
φ : Flow coefficient (= $Q/(\Omega r_2^3)$)
Ω : Angular speed, rad/s

Subscripts

2 : Impeller exit
4 : Diffuser vane inlet
4M : 4M measurement location
8M : 8M measurement location
max : Maximum
min : Minimum

Superscripts

- : Time average
' : Fluctuation

References

[1] K. U. Ziegler, H. E. Gallus and R. Niehuis, A study on impeller-diffuser interaction part I: influence on the performance, *Journal of Turbomachinery*, 125 (1) (2003) 173-182.

[2] K. U. Ziegler, H. E. Gallus and R. Niehuis, A study on impeller-diffuser interaction part II: detailed flow analysis, *Journal of Turbomachinery*, 125 (1) (2003) 183-192.

[3] Y. K. P. Shum, C. S. Tan and N. A. Cumpsty, Impeller-diffuser interaction in a centrifugal compressor, *Journal of Turbomachinery*, 122 (4) (2000) 777-786.

[4] P. Gaetani, G. Persico, A. Mora, V. Dossena and C. Osnaghi, Impeller-vaned diffuser interaction in a centrifugal compressor at the best efficiency point, *ASME Turbo Expo 2011*, Vancouver (2011) 2087-2097.

[5] P. Gaetani, G. Persico, A. Mora, V. Dossena and C. Osnaghi, Impeller-vaned diffuser interaction in a centrifugal compressor at off design conditions, *ASME Turbo Expo 2011*, Vancouver (2011) 2099-2110.

[6] C. J. Smythe, Forced response predictions in modern centrifugal compressor design, *Master's Thesis*, Massachusetts Institute of Technology, USA (2005).

[7] V. Villanueva, Characterization of the flow field response to vaneless space reduction in centrifugal compressors, *Master's Thesis*, Massachusetts Institute of Technology, USA (2006).

[8] K. A. Gould, C. S. Tan and M. Macrorie, Characterization of unsteady impeller-blade loading in a centrifugal compressor with a discrete-passage diffuser, *ASME Turbo Expo 2007*, Montreal (2007) 1781-1790.

[9] A. Zemp and R. S. Abhari, Vaned diffuser induced impeller blade vibrations in a high-speed centrifugal compressor, *Journal of Turbomachinery*, 135 (2) (2013) 021015.

[10] K. U. Ziegler, Experimentelle untersuchung der laufrad-diffusor-interaktion in einem radialverdichter variabler geometrie, *Doctoral Thesis*, RWTH Aachen University, Germany (2003).
[11] S. Connell, M. Braaten, L. Zori, R. Steed, B. Hutchinson and G. Cox, A comparison of advanced numerical techniques to model transient flow in turbomachinery blade rows, *ASME Turbo Expo 2011*, Vancouver (2011) 1241-1250.
[12] S. Connell, B. Hutchinson, P. Galpin, R. Campregher and P. Godin, The efficient computation of transient flow in turbine blade rows using transformation methods, *ASME Turbo Expo 2012*, Copenhagen (2012) 2631-2640.
[13] Q. Huang, X. Zheng and A. Wang, Mechanism and flow control on the mismatching of impeller and vaned diffuser caused by inlet prewhirl for centrifugal compressors, *ASME Turbo Expo 2016*, Seoul (2016) V02DT42A007.
[14] Y. Liu, B. Liu and L. Lu, Investigation of unsteady impeller-diffuser interaction in a transonic centrifugal compressor stage, *ASME Turbo Expo 2010*, Glasgow (2010) 1961-1971.
[15] R. C. Dean and Y. Senoo, Rotating wakes in vaneless diffusers, *Journal of Basic Engineering,* 82 (1960) 563-574.
[16] M. Schleer and R. S. Abhari, Clearance effects on the evolution of the flow in the vaneless diffuser of a centrifugal compressor at part load condition, *Journal of Turbomachinery*, 130 (3) (2008) 031009.

Dongjae Kong is a Ph.D. student at the Department of Mechanical Engineering, Stanford University. He received his B.S. and M.S. in Mechanical Engineering from Seoul National University. Before joining Stanford University, he was a full-time lecturer at the Department of Aerospace Engineering, Korea Air Force Academy. His research interest now covers thermochemistry, electrochemistry, and nanomaterials for energy applications.

Seung Jin Song is a Professor at the School of Mechanical and Aerospace Engineering, Seoul National University. He received S.M. and Sc.D. in Aeronautics and Astronautics from MIT. His current research interests include aerodynamics and fluid-structure interactions in turbomachinery, cavitation in rocket turbopumps, analysis of propulsion/power generation systems, and related areas of fluid mechanics.